APPLIED SCIENCE AND ENGINEERING

Low-power microelectronics embedded in live jellyfish enhance propulsion

Nicole W. Xu[1] and John O. Dabiri[2,3]*†

Artificial control of animal locomotion has the potential to simultaneously address longstanding challenges to actuation, control, and power requirements in soft robotics. Robotic manipulation of locomotion can also address previously inaccessible questions about organismal biology otherwise limited to observations of naturally occurring behaviors. Here, we present a biohybrid robot that uses onboard microelectronics to induce swimming in live jellyfish. Measurements demonstrate that propulsion can be substantially enhanced by driving body contractions at an optimal frequency range faster than natural behavior. Swimming speed can be enhanced nearly threefold, with only a twofold increase in metabolic expenditure of the animal and 10 mW of external power input to the microelectronics. Thus, this biohybrid robot uses 10 to 1000 times less external power per mass than other aquatic robots reported in literature. This capability can expand the performance envelope of biohybrid robots relative to natural animals for applications such as ocean monitoring.

INTRODUCTION

Jellyfish are compelling model organisms for more energy-efficient underwater vehicles because of their low cost of transport (COT; or mass-specific energy input per distance traveled) (1). Existing robotic mimics of swimming animals composed entirely of engineered components can achieve velocities comparable to natural animals, but with orders of magnitude less efficiency than jellyfish (2–7). In contrast, biohybrid jellyfish robots that incorporate live animals offer potential advantages that address the grand challenges of robotics (8), by using the jellyfish structure and muscle for actuation, solving the power requirements by leveraging natural feeding behaviors to extract chemical energy from prey in situ, and recovering from damage via wound healing processes that are inherent to the animal. This robotic approach to controlling animal locomotion can also enable further studies of live organism biomechanics in user-controlled experiments. Thus, a biohybrid robot that uses a system of microelectronics to externally control swimming in live jellyfish can advance both the science and engineering of aquatic locomotion.

Leveraging biology to address challenges in robotics

Actuation and power consumption remain two primary limitations of robotic systems. Yang et al. (8) highlight biohybrid and bio-inspired soft robots as a means to improve robotics, using biological organisms as a gold standard of performance. Potential advances include batteries that match low metabolic energy expenditures in animals, muscle-like actuators, and self-healing and self-manufacturing materials (8). Currently, mechanical soft robots that mimic fish and jellyfish propulsion leverage engineered materials. However, these biomimetic robots exhibit higher energy consumption than their animal counterparts and are therefore typically

tethered to external power supplies (3, 7). In contrast, biological soft robots require less power. Examples of these bottom-up approaches include artificial jellyfish and rays made from rat cardiomyocytes seeded on silicon scaffolds (9, 10), as well as robots that incorporate skeletal muscle, collagen, and sea slug tissue cultures for additional features, such as speed and controllability (11–13). However, such biological robots are limited to swimming in cell medium cultures for survival.

By using live jellyfish as a natural scaffold, we can use the animals' own basal metabolism to reduce power requirements, leverage its muscles for actuation, and rely on self-healing and regenerative tissue properties for increased damage tolerance. Although more work is needed to improve the maneuverability of robots that use live animals, in this work, we have constructed a biohybrid robot that is 10 to 1000 times more energy efficient than existing swimming robots reported in literature, by integrating microelectronics in live jellyfish.

Using robotics to address open questions in biology and ecology

Because jellyfish are naturally found in a wide range of salinities, temperatures, oxygen concentrations, and depths (including 3700 m or deeper in the Mariana Trench) (14, 15), these biohybrid robots also have the potential to be deployed throughout the world's oceans. Because biologging larger marine animals has been shown to expand the capabilities of ocean observations (16), the user control of jellyfish could further expand ocean monitoring and robotic sampling as an additional resource to current work using autonomous underwater vehicles (AUVs) (17) and hydroacoustics (18).

Jellyfish swimming also provides a source of inspiration for studying basic science questions regarding animal-fluid interactions (19, 20). Because locomotion is required for jellyfish to feed, escape predators, and reproduce (21, 22), their biomechanics and ecology are intimately connected, with implications for phenomena such as jellyfish blooms (23). However, current studies of jellyfish are limited to observations of endogenous swimming. User control of swimming could enable a much broader range of studies of the biology and ecology of animal locomotion in laboratory and in situ experiments.

[1]Department of Bioengineering, School of Engineering and School of Medicine, Stanford University, Stanford, CA 94305, USA. [2]Department of Civil and Environmental Engineering, School of Engineering, Stanford University, Stanford, CA 94305, USA. [3]Department of Mechanical Engineering, School of Engineering, Stanford University, Stanford, CA 94305, USA.
*Present address: Graduate Aerospace Laboratories (GALCIT) and Mechanical Engineering, California Institute of Technology, Pasadena, CA 91125, USA.
†Corresponding author. Email: jodabiri@caltech.edu

To illustrate the power of this new approach for basic science, we hypothesized that increasing bell contraction frequencies increases swimming speeds up to a limit, in which the kinematics are compromised when the bell cannot fully relax before the next pulse, but at an energetic cost that follows a cubic power law. By externally controlling the frequency of pulses in free-swimming animals and by measuring the corresponding swimming speed and oxygen consumption, we calculated the COT to test the aforementioned hypothesis in this work. Such an examination was previously only possible in theoretical or computational models.

Aurelia aurita as a model organism

Figure 1 summarizes our scheme for controlled swimming in jellyfish. *Aurelia aurita* is an oblate species of jellyfish comprising a flexible mesogleal bell and monolayer of coronal and radial muscles that line the subumbrellar surface (see schematic in Fig. 1D). To swim, the muscles contract to decrease the subumbrellar cavity volume and eject water to provide motive force (*21, 22, 24, 25*), with additional contributions to forward motion from passive energy recapture (*1*) and suction-based propulsion (*26*). To initiate these muscle contractions, the animal activates any of its eight pacemakers, located within rhopalia (sensory organs) along the bell margin. These nerve clusters activate the entire motor nerve net and cause bidirectional muscle wave propagations originating from the activated pacemakers (*21, 22, 24, 25, 27–31*).

Previous electrophysiology studies have shown that applying a periodic electric current can incite rhythmic muscle contractions in constrained medusae, but the specific input-output responses—from electrical stimulation to muscle contraction—have not been fully described (*27–31*). We systematically characterized the spatiotemporal response of *Aurelia* to electrical signals of varying amplitudes (*A*), pulse durations (*T*), frequencies (*f*), and electrode locations to identify combinations that robustly and repeatably incite muscle contractions (see Supplementary Text and fig. S1 for further discussion). This characterization guided the design of a microelectronic system for external control of jellyfish swimming.

RESULTS

Robotic design and implementation in live jellyfish

On the basis of extensive characterization of the spatiotemporal parameter space of jellyfish muscle stimulation (see Supplementary Text and fig. S1), we created a portable, self-contained microelectronic swim controller that generates a square pulse wave (A = 3.7 V, T = 10 ms; Fig. 1A) to stimulate muscle contractions from 0.25 to 1.00 Hz. As shown in Fig. 1 (B and C), the controller is composed of a TinyLily mini-processor (TinyCircuits, Akron, OH, USA) and a 10-mAh lithium polymer cell (GM201212, PowerStream Technology Inc., Orem, UT, USA) encased in a 2.11-cm-diameter cylindrical polypropylene housing and sealed with Parafilm M Film (Bemis Company Inc., Oshkosh, WI, USA). Two wire electrodes were composed of perfluoroalkoxy (PFA)–coated silver wire with a bare diameter of 76.2 μm and a coated diameter of 139.7 μm, and platinum rod tips with a diameter of 254.0 μm (A-M Systems, Sequim, WA, USA). The wires were connected in series to TinyLily 10402 light-emitting diodes (LEDs; TinyCircuits, Akron, OH, USA) for visual confirmation of the electrical signal.

To attach the swim controller to the jellyfish, a 2.5-cm wooden pin attached to the center of the polypropylene housing was inserted
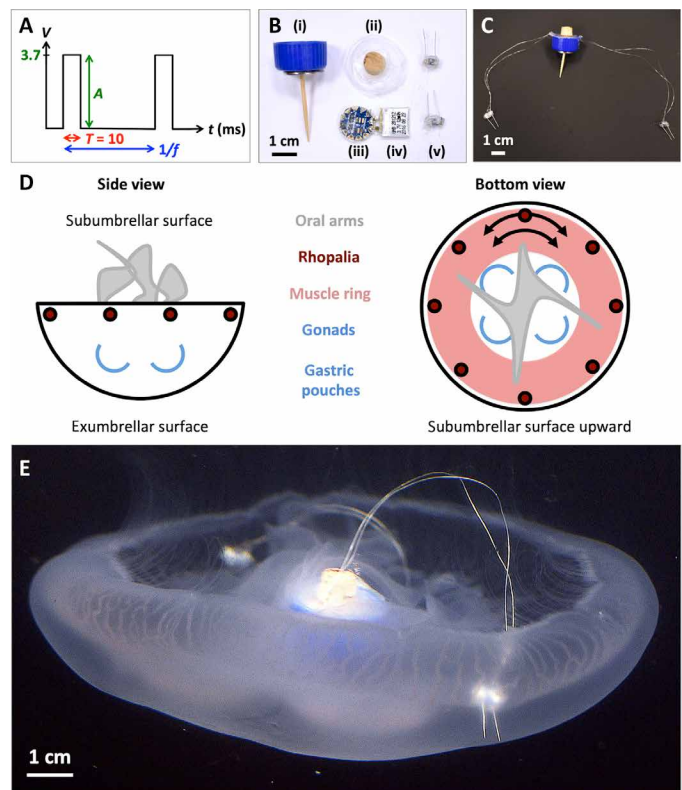

Fig. 1. *A. aurita* swim controller design. (**A**) Square wave signal generated by the swim controller with an amplitude (*A*) of 3.7 V and a pulse width (*T*) of 10 ms, set at frequencies (*f*) of 0.25, 0.38, 0.50, 0.62, 0.75, 0.88, and 1.00 Hz. (**B**) Swim controller components. Housing includes (i) a polypropylene cap with a wooden pin that embeds into the bell center, and (ii) a plastic film to waterproof the housing, both offset with stainless steel and cork weights to keep the device approximately neutrally buoyant. Microelectronics include (iii) a TinyLily mini-processor, (iv) lithium polymer battery, and (v) two platinum-tip electrodes with LEDs to visually indicate stimulation. (**C**) Fully assembled device, with the processor and battery encased in the housing. (**D**) Simplified schematics of *A. aurita* anatomy, highlighting the subumbrellar (top) and exumbrellar (bottom) surfaces, rhopalia, muscle ring, and circumferential muscle fiber orientation, oral arms, and gonads/gastric pouches. (**E**) Swim controller (inactive) embedded into a free-swimming jellyfish, bell oriented subumbrellar side up, with the wooden pin inserted into the manubrium and two electrodes embedded into the muscle and mesogleal tissue near the bell margin. Photo credits for (B), (C), and (E): Nicole W. Xu, Stanford University.

into the manubrium of the bell, on the subumbrellar side of the bell center. Electrodes were inserted bilaterally into the subumbrellar tissue midway between the bell margin and center (Fig. 1E, jellyfish oriented subumbrellar surface upward). The system weight was offset with stainless steel washers and cork to keep the system approximately neutrally buoyant.

Device validation

To validate that the swim controller can externally drive jellyfish bell contractions, we developed a method to track motion of the bell margin. *A. aurita* medusae were placed subumbrellar surface up in a plate without seawater, with tags injected into the tissue (red dots, circled in Fig. 2A; see Materials and Methods). From tag displacements, such as the example curves shown in Fig. 2 (B to D), we calculated the single-sided amplitude spectrum (SSAS) to obtain the
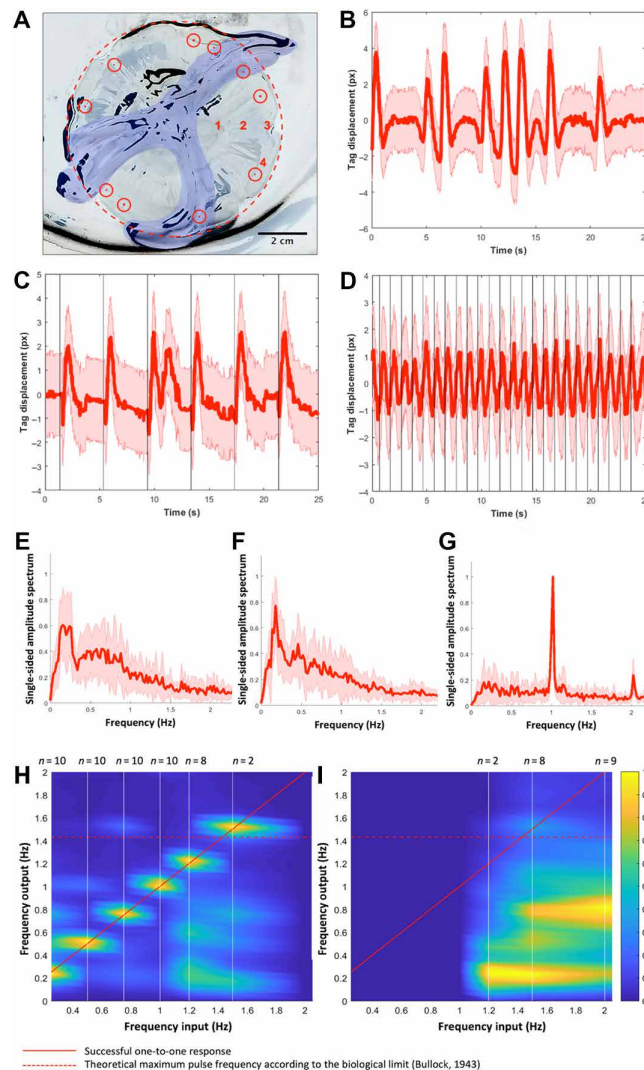
Fig. 2. Signal validation using visual tags and frequency spectra to track muscle contractions. (**A**) *A. aurita* medusae (*n* = 10, 8.0 to 10.0 cm in diameter) were placed subumbrellar surface up in a plate without seawater for constrained muscle stimulation experiments (electrode not shown). The image is inverted so that the bell and plate are white, and black areas are reflections of light from animal tissue and the plate. For clarity, the margin of the bell is outlined in a red dotted circle, and the oral arms are colorized in blue. Visible implant elastomer tags (shown as colored red dots within red circles) were injected around the margin, and one tag was tracked per video to calculate the tissue displacement as a surrogate for muscle contractions. Spatial tests to determine whether electrode location affected the spectra were conducted at four locations, labeled in red numbers: (1) adjacent to the gastric pouches, (2) midway between the gastric pouches and margin, (3) at the rhopalia, and (4) at the margin away from the rhopalia (see "Extended results" sections in Supplementary Text). All other tests were conducted at location 2. (**B**) Example tag displacement as a function of time for an animal without any external stimulus. The red line indicates the centroid displacement, with the error calculated from assuming a half-pixel uncertainty in finding the centroid of the tag in each image, over 25 s. Note the temporal variation of muscle contractions, including periods of regular pulses and successive rapid pulses. (**C**) Example tag displacement for an animal with an external stimulus of 0.25 Hz, with each stimulus visualized as a vertical black line. Although contractions regularly follow external stimuli, natural animal pulses also occur at low frequencies. Note, for example, the double pulse after one stimulus (*t* ≈ 12 s). (**D**) Example tag displacement for an animal with an external stimulus of 1.00 Hz, with each stimulus visualized as a vertical black line. The same time window (25 s) is shown for a fair comparison to the previous two plots. Contractions regularly follow external stimuli. (**E**) SSASs averaged for jellyfish without any external stimulus (*n* = 12 for 10 animals, i.e., 2 jellyfish had two replicate clips each). The red line indicates the mean of normalized SSAS for each replicate, with the SD in pink. The peak of the mean SSAS is at 0.16 Hz. The FWHM is 0.24 Hz. (**F**) Jellyfish response to an inactive electrode embedded (*n* = 14 for 10 animals, i.e., 4 jellyfish had two replicate clips each). The peak of the mean SSAS is at 0.18 Hz. The FWHM is 0.16 Hz. Using a two-sample *t* test of the peak frequencies for both groups, the difference between the two samples was statistically insignificant (*P* = 0.68). (**G**) Sample SSAS for an electrical stimulus at 1.00 Hz (*n* = 10 jellyfish for an input signal of 4.2 V and 4.0 ms). The peak frequency occurs at 1.02 Hz, within the 0.02 window used to calculate the SSAS. Note that the spectrum has a sharper peak at the frequency of interest (FWHM of 0.04 Hz), as opposed to a wider FWHM in (B) and (C), the cases without any external stimulus. (**H**) Contour map of the frequency response of muscle contractions to external electrical stimuli. Each vertical line of data (centered on white lines at 0.25, 0.50, 0.75, 1.00, 1.20, 1.50, and 2.00 Hz) represents the PSD at one electrical input frequency, with the number of jellyfish tested shown above. The colors correspond to the amplitude of the PSD, in which higher values are shown in yellow and lower values in blue. The solid red line represents a one-to-one input-output response, and the dashed red line represents the reported physiological limit according to the minimum absolute refractory period of *A. aurita* muscle (*32*). Responsive trials are defined by whether the peak frequencies in the PSD lie within a window of 0.06 Hz of the solid red curve. (**I**) Contour maps of the unresponsive trials. Higher frequencies up to 90.00 Hz were also tested with similar unresponsive PSDs. Photo credit for (A): Nicole W. Xu, Stanford University.

mean peak and mean full width at half maximum (FWHM) of bell contractions over time.

Three sets of experiments were conducted: controls to directly observe the animals' endogenous contractions in the absence of any perturbations, controls to observe whether mechanically embedding inactive electrodes would affect natural animal behavior, and stimulation protocols to confirm externally driven contractions.

Endogenous contractions (natural animal behavior)

Natural contractions were irregular with high pulse rate variability (Fig. 2B). Measurements indicated a mean peak frequency value of 0.16 Hz and an FWHM of 0.24 Hz for $n = 12$ (10 animals, with two replicates each for 2 of the animals), as shown in Fig. 2E. The FWHM reflected natural inter-animal and intra-animal variation of endogenous swimming.

An inactive electrode was tested to determine whether insertion affected the bell contraction frequency. This resulted in a mean peak frequency value of 0.18 Hz and an FWHM of 0.16 Hz, as shown in the mean SSAS in Fig. 2F, for $n = 14$ (10 animals, with two replicates each for 4 of the animals). The difference between the two mean peak values was statistically insignificant using a two-sample t test ($P = 0.68$). This suggests that the frequency spectra are not significantly changed by mechanical artifacts from implanting the electrode, i.e., any statistically significant changes to the frequency spectra of externally stimulated animals are due to external electrical stimulation.

Externally driven contractions

In comparison to the animals' endogenous pulses, which occur naturally without external stimuli, externally driven contractions resulted in tag displacement curves shown in Fig. 2C (driven at 0.25 Hz) and Fig. 2D (driven at 1.00 Hz). Black vertical lines indicate each single square pulse stimulus (Fig. 1A), which underscores the regularity of muscle contractions post-stimulus. However, variations do occur, such as the endogenous bell contraction in the 0.25-Hz test (Fig. 2C, $t \approx 12$ s). See the "Limitations" section in Supplementary Text for further discussion.

For an externally driven frequency input of 1.00 Hz, the normalized SSAS is shown in Fig. 2G, featuring a sharp, narrow peak at the driven frequency. Note that compared to the endogenous SSAS curves in Fig. 2 (E and F), this peak is narrower (i.e., FWHM = 0.04 Hz), reflecting more regular bell contractions.

Externally driven contraction frequency map

The frequency response of the animal contractions to external electrical stimulation is plotted as a contour map in Fig. 2 (H and I), in which discrete vertical lines (shown in white) represent power spectral densities (PSDs) for each electrical frequency input. The number of trials corresponding to each vertical PSD column is listed above each data line. The map is colored by the amplitude of the mean normalized PSD (with interpolated values between data lines), from higher amplitudes in yellow to lower amplitudes in blue. The solid red line indicates a one-to-one response, i.e., if a peak occurs within 0.06 Hz of the input frequency. This band is the windowing error based on the resolution of the PSD. The dashed red line indicates the reported physiological limit of jellyfish muscle contractions at 1.4 Hz, according to the observed absolute refractory period of *A. aurita* muscle (*29*). We observe that the muscle can respond slightly above this limit (i.e., 1.50 Hz).

As plotted, one-to-one input-output responses were observed for each tested stimulation frequency of up to 1.00 Hz (Fig. 2H). From 1.20 to 2.00 Hz, the number of responsive cases decreased

until all jellyfish tested did not respond at frequencies above 1.50 Hz. These unresponsive cases showed SSASs and PSDs similar to the unstimulated control cases (Fig. 2I). Higher frequencies above those shown on the contour maps were also tested, with no occurrence of tetany and similar frequency responses to those in the unstimulated control groups. The two-sample t test for SSASs at 10 Hz ($n = 8$ animals) yielded $P = 0.16$ and 0.36 compared to the two controls, respectively, and at 90 Hz ($n = 9$ animals) yielded $P = 0.46$ and 0.80. At the lowest tested frequency, 0.25 Hz, prominent secondary peaks at 0.50 Hz were observed, which were indicative of the presence of endogenous contractions (Fig. 2C, $t \approx 12$ s, see Supplementary Text).

Enhanced swimming speeds up to 2.8 times using onboard microelectronics to drive frequencies

Swimming trials with the implanted system were conducted in a 1.8 m × 0.9 m × 0.9 m saltwater tank. As illustrated in Fig. 3A, animals were introduced at the top of the tank and observed swimming downward to the bottom of the tank. We tracked bell displacements at external stimulation frequencies from 0 Hz (swim controller inactive, endogenous pulses only) to 1.00 Hz, which bracketed the observed endogenous swimming frequencies. The measured swimming speeds were normalized by the body diameter to account for variations in animal size ($n = 6$ animals). The normalized swimming speed scaled by the mean of the normalized 0-Hz speed (in the absence of stimulation) is subsequently referred to as the enhancement factor. Figure 3B plots enhancement factors and speeds, which both peaked at 0.50- or 0.62-Hz external stimulation for all jellyfish. The maximum peak enhancement factor was 2.8 ± 0.3 times the natural swimming speed of the animals.

We observed a trend correlating greater performance enhancements with smaller, less oblate jellyfish, as determined by the bell diameter and fineness ratio (i.e., bell height to diameter ratio). The maximum observed enhancement occurred for the animal with the smallest bell diameter (13.0 cm) and greatest fineness ratio (0.3). Conversely, the smallest peak enhancement (1.3 ± 0.1) occurred for the animal with the largest bell diameter (18.2 to 19.0 cm) and smallest fineness ratio (0.2).

For endogenous swimming in vertical free-swimming experiments, the natural observed swimming frequency was 0.24 ± 0.11 Hz ($n = 8$). Although this mean frequency is comparable to the controller-driven frequency of 0.25 Hz, the variability of the endogenous swimming frequency was higher (Fig. 2, E and F) compared to externally driven swimming frequencies (Fig. 2G), as previously noted. This irregular swimming results in slower overall speeds, in contrast to the higher swimming speeds observed under external stimulation at frequencies with comparable mean values to natural swimming.

With increasing swimming frequencies imposed by the controller, swimming speeds increased until a biological constraint was reached, which occurred when the driven input f was greater than a critical frequency (f_{crit}) corresponding to the sum of the contraction (t_c) and relaxation times (t_r), i.e., $f_{crit} = 1/(t_c + t_r)$. In these cases, the muscle could not fully relax to allow the subumbrellar cavity volume to refill completely before subsequent contractions (see movie S1). Hence, the amount of incremental thrust generated decreased, leading to decreasing swimming speeds at higher f values. These trends in enhancement versus body size, fineness ratio, and swimming frequency were predictable based on a new theoretical model that captures the tradeoff between faster swimming speeds and shorter
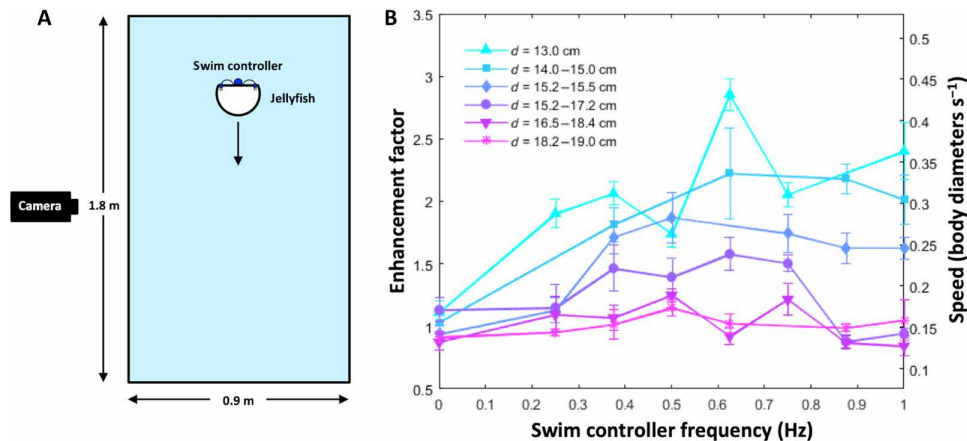
Fig. 3. Externally driven swimming can increase speeds up to 2.8 times. (**A**) Schematic of vertical free-swimming experiments. Jellyfish ($n = 6$, resting bell diameters d ranging from 13.0 to 19.0 cm) swam downward starting from rest in a 1.8 m × 0.9 m × 0.9 m artificial seawater tank. Videos were recorded using a single camera at 60 fps. (**B**) Swimming speeds and enhancement factors for swim controller frequencies at 0, 0.25, 0.38, 0.50, 0.62, 0.75, 0.88, and 1.00 Hz. Each animal is represented by a different color curve, and the size range per animal reflects changes in bell growth over time (experiments were conducted over several days). Normalized speeds (body diameters per second) are indicated on the right ordinate axis. The enhancement factor is defined as the normalized swimming speed scaled by the mean of the normalized 0-Hz speed (in the absence of stimulation, in which the swim controller is embedded but inactive).

muscle relaxation times at higher swimming frequencies (see the "Mechanistic model" section in Materials and Methods, Supplementary Text, and figs. S2 to S4). This model extends the work from previous hydrodynamic models to incorporate more biologically relevant swimming kinematics and morphological parameters, including inactive periods at lower swimming frequencies and truncated muscle contractions at higher frequencies (see the "Adaptations to the model" section in Materials and Methods for further improvements).

Device power consumption: 10 to 1000 times more energy efficient than existing aquatic robots

The artificially controlled jellyfish requires both external power from the microelectronic system and internal power from the animals' own metabolism. As a fair comparison to other robots, including bottom-up robotic constructs that incorporate cells and neglect adenosine 5′-triphosphate (ATP) consumption, we will first discuss the external power consumption of the microelectronic components, followed by a discussion of the animals' energy expenditure at externally driven frequencies.

The microelectronic system of the biohybrid robotic jellyfish consumed 0.06 ± 0.01, 0.13 ± 0.03, and 0.12 ± 0.09 W kg^{-1} when driven at 0.25, 0.50, and 0.88 Hz, respectively. Compared to existing robots, this biohybrid robot uses up to 1000 times less external power (from the 10-mAh battery in the swim controller) per mass of the biohybrid robot (comprising the animal and microelectronic system). Figure 4 illustrates a comparison of this system with swimming robots reported in literature (see table S3 for values and calculations). Marker shapes indicate the type of aquatic robot, from robots composed of biological tissue, such as the medusoid and robotic ray made from rat cardiomyocytes seeded on silicon scaffolds (9, 10), to purely mechanical robots, including bioinspired robots (3, 7, 33, 34) and AUVs (35). Marker colors indicate the type of propulsion, including medusan (jellyfish swimming), thunniform (fish swimming), rajiform (ray swimming), and propeller-driven locomotion.

The present biohybrid robotic jellyfish performs at similar swimming speeds (3.0 to 3.5 cm s^{-1}) to those of other bioinspired mechanical robots, such as Robojelly at 3.1 cm s^{-1} and Jennifish at

3.0 cm s^{-1} (3, 33). However, there is a tradeoff between normalized power consumption and speed. For example, the mechanical soft robotic fish SoFi can swim 10-fold faster but with a 100-fold increase in normalized power consumption (34). A similar trend is observed with the REMUS 100 AUV, which uses 500 W kg^{-1} to travel 1 m s^{-1} (35). Both types of underwater robots—low-power robots such as this biohybrid robot and high-power robots with faster swimming speeds such as AUVs—can be appropriate for ocean monitoring purposes. However, the present work can potentially enable newer underwater vehicles to observe the environment over significantly longer durations and, similarly to SoFi, might be used with minimal disturbances to the environment because the body form and generated wakes are similar to those of natural organisms. Moreover, because jellyfish do not have a swim bladder, they can reach 3700-m depths in the ocean (15). Only the microelectronics will require hardening for operation at high pressures.

Low cost and ease of use

In addition to low external power consumption per mass of the biohybrid robot, this microelectronic system uses less than $20 of off-the-shelf, readily available components. Furthermore, the extensive spatiotemporal characterizations conducted here enable new users to embed the device into live animals easily because electrode location is nonspecific, and animals recover immediately after experiments (see the "Ethical considerations" section in Supplementary Text).

Animal energy expenditure: 2 times increase in COT for up to 2.8 times increase in speed

Although external power for the microelectronic system is one component of the biohybrid robot's power consumption, the animal itself also expends energy. The relationship between swimming frequency and metabolic rate has not been previously studied in these organisms. The new capability for external control enables us to address this previously inaccessible question, an example of the impact of this work on basic science. The swim controller allowed a systematic frequency sweep to measure oxygen consumption rates both in animal tissue and in the surrounding water (see experimental
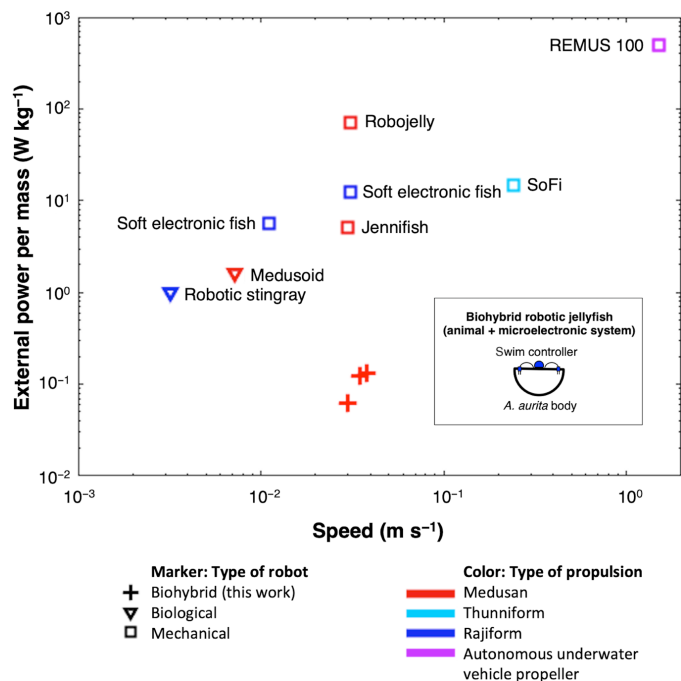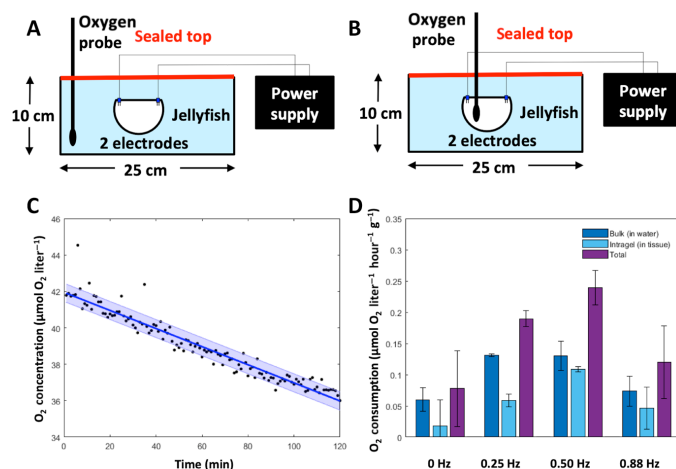
Fig. 4. External power requirements of the biohybrid robotic jellyfish compared to other swimming robots in literature. Marker shapes illustrate the type of aquatic robot, from biological soft robots such as the medusoid and robotic ray made from rat cardiomyocytes seeded on silicon scaffolds (9, 10) to mechanical robots, including bioinspired robots (3, 7, 33, 34) and an AUV (35). Marker colors illustrate the type of propulsion, including medusan (jellyfish swimming), thunniform (fish swimming), rajiform (ray swimming), and propeller-driven (AUVs). The external power (from the 10-mAh battery in the swim controller) per mass of the biohybrid robot (comprising the animal and the microelectronic system) is plotted versus swimming speed as red crosses. For actual values and details on the calculations, see table S3.


Fig. 5. Metabolic rate experiments. To determine the metabolic rate of jellyfish, oxygen concentrations were measured in animal tissue and the surrounding water and then converted into energy expenditure. (**A**) Experimental setup to measure bulk dissolved oxygen concentrations (in the water). Animals were placed submbrellar surface upward in a sealed glass dish filled with 2 liters of artificial seawater, with two electrodes for frequency-driven cases. Oxygen levels in the water were measured using a MicroOptode oxygen probe. (**B**) Experimental setup to measure intragel oxygen concentrations (in the tissue). Animals were placed subumbrellar surface upward in a sealed glass dish filled with 2 liters of artificial seawater, with two electrodes for frequency-driven cases. Intragel oxygen levels were measured using a MicroOptode oxygen probe embedded into the tissue. (**C**) Representative plot of oxygen concentrations over time, measured from the MicroOptode. This example shows measurements of bulk oxygen levels in the water surrounding an animal with a swim controller–driven frequency of 1.00 Hz. Individual data points are shown in black, the best-fit line is shown in dark blue, and the SD is shown in the light blue shaded region. (**D**) Oxygen consumption rates of the surrounding water (dark blue), within animal tissue (light blue), and total (sum of the water and tissue measurements, purple) were calculated over a 6- to 8-hour period ($n = 7$ animals).

schematic in Fig. 5, A and B, and representative curve of oxygen levels over time in Fig. 5C). Consumption rates of dissolved oxygen in the surrounding water, in the animal tissue, and the sum are shown in Fig. 5D. The consumption rates during stimulation are compared to basal metabolism, i.e., in the absence of external stimulation. Oxygen consumption rates followed a similar pattern to enhanced swimming speeds: Respiratory rates increased from 0 to 0.50 Hz and then decreased at the highest tested frequency of 0.88 Hz.

We calculated the equivalent COT using both experimental metabolic rates and experimental swimming speeds. Figure 6 shows these experimental COTs in black. The baseline COT (experimental values at 0 Hz, without active user swim control) matched previously reported *A. aurita* COT values, visualized in blue in Fig. 6 (*1*). Experimental COT follows a similar pattern to the underlying oxygen consumption rates, increasing at mid-range frequencies, and decreasing at high external stimulation frequencies.

Measured COT increases twofold at 0.25 and 0.50 Hz compared to the baseline value and 0.88 Hz. This is within the same order of magnitude as the two model predictions. The power law model used experimental swimming speed data, with the assumption that power scales cubically with speed. The mechanistic model, developed to investigate the effects of animal size and fineness ratio (Supplementary Text and figs. S2 to S4), used no experimental data input aside from morphological parameters (see Materials and Methods).

The experimental COT at 0.25 Hz was higher than both predicted COTs, likely due to the presence of endogenous pulses, as previously described (Fig. 2C). However, the experimental COT was lower than predicted at 0.50 and 0.88 Hz (Fig. 6), which suggests the potential for more energy-efficient swimming at faster speeds, limitations in the experimental setup necessary to measure oxygen consumption (see the "Limitations" section in Supplementary Text), or possibly a breakdown in the model assumptions.

Regardless, these results show that at externally driven frequencies higher than naturally occurring swimming frequencies, we can increase the peak speed of jellyfish swimming up to 2.8 times, with only a twofold increase in energy expenditure. In other words, the enhanced jellyfish swimming does not create undue cost to the animals' metabolism or health. The power consumption of the animal is relatively stable, as shown in the blue shaded region of fig. S5. Compared to the power consumption of the animal, the microelectronic system requires approximately the same power at 0.25 Hz and more power at higher frequencies.

DISCUSSION

The presence of efficient enhanced propulsion suggests that *A. aurita* have latent swimming capabilities, because increasing swimming speeds do not result in disproportionally high gains in animal energy
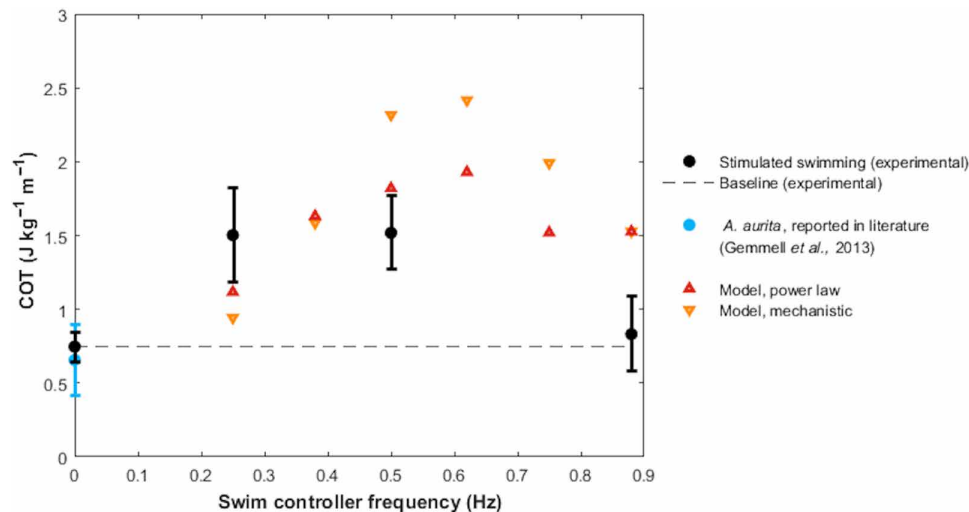
Fig. 6. Animal COT. The mean and SD of COT values (plotted in black) were calculated using experimental data from metabolic rate experiments and free-swimming speed experiments at 0 Hz (without the swim controller) and 0.25, 0.50, and 0.88 Hz (with the active swim controller). The experimentally calculated COT at 0 Hz is labeled as the baseline (horizontal black dashed line). The baseline values match experimental data reported in literature for *A. aurita*, in blue (*1*). Triangular markers indicate model estimates of COT. Values plotted in red were calculated assuming a cubic relationship between power and speed, using experimental data from free-swimming experiments (but no metabolic data). Values plotted in orange were calculated from a mechanistic model, adapted from literature (no experimental data) (*20, 42*).

expenditure. Because enhanced propulsion is not naturally exhibited by this species, external stimulation has been required to discover these capabilities. A possible explanation for the existence of more proficient and efficient swimming at nonnatural bell contraction frequencies stems from the multipurpose function of vortices shed during swimming. Vortex formation serves not only for locomotion but also to enable filter feeding and reproduction (*36–38*). There may therefore be no evolutionary pressure for *A. aurita* to use its full propulsive capabilities in nature, and there is apparently no significant cost associated with maintaining those capabilities in a dormant state, although higher speeds might limit the animals' ability to feed as effectively.

More broadly, a longstanding limitation of animal studies is user reliance on natural animal behavior, which usually does not allow for systematic exploration of the design space of animal locomotion. Although this method does not arrest endogenous animal contractions (see the "Limitations" section in Supplementary Text), the method could also be used in similar experiments to test the effects of muscle contraction rates on tissue repair and morphology (*39*). This biohybrid robotics approach could enable further studies of whole live organisms in more user-controlled, rigorous experiments that were previously inaccessible.

For robotic applications, wherein maximum propulsion may be a priority, the discovered latent enhanced performance could be exploited to circumvent longstanding limitations of engineered robots, such as the materials performance, control, and power requirements. In the present case, we obtained a 2.8 times increase in swimming speed for an external input of only 10 mW to power the device components.

The main robotic limitation is the power requirement of the microelectronic system, as underscored in the comparison of animal versus microelectronic power needs in fig. S5. Although animal power consumption is relatively insensitive to swimming frequency and the normalized power requirements of the entire biohybrid robot are still orders of magnitude less than existing robots, future improvement to the microelectronics can further decrease energetic

costs. Extended studies should also strive to arrest endogenous animal contractions without harm to the organisms, to improve the controllability of biohybrid robots that use live animals. Future work should also explore asymmetric electrode activation to cause bell pitching and improve the maneuverability of this biohybrid robot. Nevertheless, the artificial control of jellyfish has the potential to expand ocean monitoring techniques, and future iterations of the biohybrid robotic jellyfish can improve controllability, incorporate microelectronic sensors, and leverage existing tagging technology (*16*).

MATERIALS AND METHODS
Animal husbandry
A. aurita medusae were obtained from Cabrillo Marine Aquarium (San Pedro, CA, USA). Specimens were maintained at 21°C in a 453-liter grow-out pseudokreisel tank (Jelliquarium 360, Midwater Systems, Thousand Oaks, CA, USA) filled with artificial seawater composed of sea salt mix (Instant Ocean Sea Salt, Spectrum Brands, Blacksburg, VA, USA) and deionized water at 35 ppt (parts per thousand). The jellyfish were fed daily with naupliar *Artemia franciscana* (Hatching Shell-Free Brine Shrimp Eggs E-Z Egg, Brine Shrimp Direct, Ogden, UT, USA). Batches of brine shrimp were hatched from eggs using artificial seawater (35 ppt, initially at 27°C until hatched, and maintained at room temperature, 21°C), enriched every other day with SELCO (Self-Emulsifying Lipid Concentrate, Brine Shrimp Direct, Ogden, UT, USA).

Spatiotemporal response to electrical stimuli experiments
Wire electrodes composed of PFA-coated silver wire with a bare diameter of 76.2 μm and a coated diameter of 139.7 μm, and platinum rod tips with a diameter of 254.0 μm (A-M Systems, Sequim, WA, USA) were connected to a MyoPacer cell stimulator (IonOptix, Westwood, MA, USA) as a power source to generate square pulse waveforms with variable voltage amplitudes (*A*), pulse widths (*T*), and frequencies (*f*), as shown in Fig. 1A.

Medusae (*n* = 10, 8.0 to 10.0 cm in diameter) were placed sub-umbrellar surface up in a melamine plate without seawater (Fig. 2A). Red visible implant elastomer tags (Northwest Marine Technology, Shaw Island, WA, USA) were injected into the tissue to track tissue displacement with each muscle contraction (Fig. 2, B to D). When used, electrodes were embedded perpendicular to the tissue surface.

Two negative control cases were tested to determine the natural response of jellyfish pulsing and the mechanical effect of electrode insertion. The first case observed animals without an electrode to obtain the natural frequency spectra of pulses (Fig. 2E). The second case observed animals with one inactive electrode embedded to ensure that any changes to the spectra in experimental groups would be from electrical stimulation, not from mechanical artifacts, and to determine the isolated effect of implanting the electrode (Fig. 2F).

In-dish experiments tested four variables: spatial electrode placement, signal frequency, signal amplitude, and signal pulse width. Spatial tests were conducted at four locations to determine whether differences existed in the stimulation spectra. Locations, visualized by the numbers in Fig. 2A, are defined as (1) adjacent to the gastric pouches, (2) midway between the gastric pouches and margin, (3) at the rhopalia, and (4) at the margin away from the rhopalia. The electrical signal was periodic at 1.00 Hz and 4.2 V with a pulse width of 4 ms (modified version of Fig. 1A).

For frequency, amplitude, and pulse width tests (see values in table S1), the electrode was embedded into location 2, 3, or 4, with no appreciable differences based on electrode placement (see "Extended results" sections in Supplementary Text).

Videos of jellyfish pulses were recorded on Cyber-shot DSC-RX100 (Sony Corporation of America, New York City, NY, USA) at 60 fps (frames per second) to obtain the displacement of one tag per clip relative to its starting point in a reference image (an image selected within a 1.00-s window in which the animal was stationary and relaxed) using MATLAB (MathWorks). The displacement was calculated by subtracting a moving average (using 6.67 s for 50.00-s clips and 1.67 s for 16.67-s clips) from the total displacement to isolate the motion caused by muscle contractions from large-scale motion of the bell within the plate.

To identify the peak frequencies in the displacement signal, a SSAS (i.e., the positive frequency values of the fast Fourier transform) and PSD were calculated using the Welch's method (dividing the displacement line series into a maximum of eight segments with 50% overlap, truncated if necessary, using a Hamming window). SSASs were used to compare values of the peak frequencies (Fig. 2, E to G), and PSDs were used for better visualization, by reducing noise and resolution, in a contour map plotting the electrical signal input frequencies versus muscle contraction output frequencies (Fig. 2, H and I). The SSAS and PSD were normalized from 0 to 1 for each individual animal before plotting the mean and SD of the spectra for all animals within the test group. Control, spatial, and frequency tests were analyzed using 50.00-s clips, recorded at 60 fps; voltage and pulse width tests were analyzed using 16.67-s clips recorded at 60 fps, which was a sufficient timescale to detect peak frequencies of the SSAS given a 1.00-Hz stimulation. Tests of statistical significance were performed using a two-tailed, two-sample *t* test at the peak frequency for each individual SSAS.

Immunohistochemical staining

In conjunction with the spatial tests (see the "Extended results: Characterizing animal response to electrical signals" section in Sup-

plementary Text), actin-phalloidin stains were conducted to determine the muscle orientation of selected *A. aurita* medusae with a bell diameter of >7.0 cm. These experiments answer whether the electrode was embedded into circumferentially oriented muscle, radially oriented muscle, or mesoglea only at the four locations in Fig. 2A.

For each animal (*n* = 6; bell diameter, 7.0 to 10.0 cm), a strip of tissue was excised from the edge of the gastric pouch to the margin, as illustrated in fig. S1D. Some samples contained a single rhopalium, which did not affect the results of the general orientation of muscle striations. Cut animals recovered after excision.

Actin-phalloidin stains were performed following an adapted method from Yuan *et al.* (*40*). Tissue sections were soaked in a 1:2 solution of 1 M magnesium chloride ($MgCl_2$) (Ambion, Invitrogen, Thermo Fisher Scientific, Waltham, MA, USA) in 34 ppt of artificial seawater for 5 min, fixed in 4% paraformaldehyde in 1× phosphate-buffered saline (PBS) (Alfa Aesar, Haverhill, MA, USA) for 1 hour, and washed six times in 1× PBS (pH 7.4) (Gibco, Thermo Fisher Scientific, Waltham, MA, USA). The sections were then permeabilized in 0.3% Triton X-100 (Fisher BioReagents, Thermo Fisher Scientific, Waltham, MA, USA) in 1× PBS (PBSTr) for 2 hours, blocked in normal goat serum (Rockland Immunochemicals, Pottstown, PA, USA) for 1 hour, and washed six times in PBSTr. Last, the tissue was stained overnight (12 to 24 hours) in 1:20 dilutions of Alexa Fluor 488 phalloidin (Invitrogen, Thermo Fisher Scientific, Waltham, MA, USA) in PBSTr, washed in 1× PBS, and stored in 4°C for imaging within 1 week with no observed signal loss. The tissue pieces were then imaged with an inverted Zeiss LSM 780 multiphoton laser scanning confocal microscope (Zeiss, Oberkochen, Germany).

Portable design

For free-swimming experiments, we designed a wireless microelectronic swim controller, as described in the "Robotic design and implementation in live jellyfish" section. A pulse width of 10 ms was chosen instead of 4 ms for improved visualization of electrode activation, after validating that both pulse widths produced statistically similar results. (See "Extended results" sections in Supplementary Text. For further discussion about attachment methods, see the "Ethical considerations" section in Supplementary Text.)

Vertical free-swimming experiments to determine swimming speed versus frequency

Jellyfish (*n* = 6, bell diameters from 13.0 to 19.0 cm) swam down a vertical tank of dimensions 1.8 m × 0.9 m × 0.9 m, as shown in Fig. 3A. Animals were initiated from rest, bell oriented subumbrellar surface upward, at the top of the tank. Videos were taken from one view using Cyber-shot DSC-RX100 at 60 fps. Animals were allowed to swim downward at frequencies driven by the swim controller: off (0 Hz) for control trials and 0.25, 0.38, 0.50, 0.62, 0.75, 0.88, and 1.00 Hz for experimental trials. Centroids of either the blue polypropylene housing on a white background or the entire jellyfish bell on a black background were obtained using MATLAB. Morphological and kinematic parameters were obtained using ImageJ (National Institutes of Health). Speeds were calculated from centroid displacements and normalized by the body diameter of the animal. Error bars represent 1 SD.

Metabolic rate experiments

To determine animal energy expenditure, medusae (*n* = 7) were placed subumbrellar surface upward in 2 liters of artificial seawater

in a Pyrex 190 × 100 mm glass dish. To measure endogenous respiratory rates, oxygen concentrations were recorded without embedded electrodes, without external stimuli from the swim controller. To measure respiratory rates at externally driven frequencies, two electrodes were embedded using the same technique as described in the "Spatiotemporal response to electrical stimuli experiments" section. Oxygen concentrations were measured using a microoptode (Oxygen MicroOptode 430 μm OPTO-430, Unisense, Denmark), as shown in Fig. 5C. Both bulk dissolved oxygen concentrations (in the water, see Fig. 5A) and intragel oxygen concentrations (within the animal tissue, see Fig. 5B) were measured. The top of the dish was sealed using plastic wrap directly on the water surface to minimal air above the surface. Oxygen consumption rates were measured before the surface was sealed and after 6 to 8 hours of animal consumption, with a sample measurement shown in Fig. 5C.

COT versus frequency
Total respiratory rates, using the combined bulk dissolved oxygen and intragel oxygen concentrations, were subsequently converted to energy using a factor of 19 J ml^{-1} of O_2 (41). Experimental COT values were calculated by using the energy values from metabolic experimental data and speeds from vertical free-swimming experimental data.

Power law model for COT
To compare to the experimental COT values, a power law model was used using the baseline COT (at 0 Hz, i.e., the experimental COT calculated with the swim controller was embedded but off). Power law model COTs were calculated at 0.25, 0.38, 0.50, 0.62, 0.75, and 0.88 Hz, assuming that power scales cubically with speed and inputting speeds from vertical free-swimming experimental data. No metabolic information was input into the model.

Mechanistic model
This work extends upon previous hydrodynamic models (20, 42) to calculate the velocity (u) from a momentum balance using thrust (T), drag (D), acceleration reaction (AR), and the combined force ($\sum F$). Beginning from Newton's second law where m_j is the mass of the jellyfish

$$\sum F = m_j \frac{du}{dt} \qquad (1)$$

The drag and acceleration reaction are assumed to oppose thrust. Hence

$$T - D - AR = m_j \frac{du}{dt} \qquad (2)$$

where the force components are

$$T = \left(\frac{\rho_w}{A_{sub}}\right)\left(\frac{dV_{sub}}{dt}\right)^2 \qquad (3)$$

$$D = \frac{1}{2} C_d \rho_w A_j u^2 \qquad (4)$$

$$AR = \alpha \rho_j V_j \frac{du}{dt} \qquad (5)$$

where $\rho_w = 1.024$ g/cm^3 is the density of saltwater at 35 ppt and 21°C, A_{sub} is the area of the subumbrellar opening, V_{sub} is the volume of the subumbrellar cavity, $C_d = 0.42$ is the drag coefficient for a hemisphere at a Reynolds number of 325, A_j is the area of the

jellyfish bell, $\alpha = \left(\frac{2h_t}{d_j}\right)^{1.4}$ is the added mass coefficient defined as a function of the instantaneous bell height (h_t) and diameter (d_j), and ρ_j and V_j are the density and volume of the jellyfish.

Substituting Eqs. 3 to 5 into Eq. 2 and rearranging gives

$$\left(\frac{\rho_w}{A_{sub}}\right)\left(\frac{dV_{sub}}{dt}\right)^2 = \frac{1}{2} C_d \rho_w A_j u^2 + (1 + \alpha) m_j \frac{du}{dt} \qquad (6)$$

Equation 6 was solved using dsolve in MATLAB to simulate swimming from rest for up to 15 periods. Mean speeds were calculated using the last swimming period.

Adaptations to the model
We simplified the bell as a hollow oblate hemiellipsoid, as shown in fig. S2A, with input parameters to set the morphological and kinematic parameters. Morphological parameters included the relaxed bell height (h_r), relaxed bell diameter (d_r), maximum change in height between contraction and relaxation states (Δh), maximum change in diameter between relaxation and contraction states (Δd), jellyfish tissue height (h_j), and a geometric scaling factor (s) to examine how proportionally scaling the geometry affected swimming speeds at a given fineness ratio (defined as the ratio of the bell height to the diameter). Time-dependent parameters included the contraction time (t_c), defined as the time to transition from a relaxed state to a contracted state, and the relaxation time (t_r), the time to transition from a contracted state to a relaxed state.

These parameters were input to determine a function $k(t)$ used to calculate the bell geometry at each time step (30 Hz). Note that swimming was characterized into two regimes based on a critical frequency based on the contraction and relaxation times, $f_{crit} = 1/(t_c + t_r) = 1/\tau_{crit}$. For cases when the swim frequency $f \leq f_{crit}$, $k(t)$ was defined as a Heaviside sinusoid with an idle period, $t_{idle} = 1/f - \tau_{crit}$ (fig. S2B). For cases when $f > f_{crit}$, when the swim frequency does not allow for full bell relaxation before the subsequent contraction, $k(t)$ was defined as a truncated sinusoid (fig. S2D). Using this input function, the instantaneous height $h_t = h_r + \Delta h\, k(t)$ and diameter $d_t = d_r - \Delta d\, k(t)$ (examples shown in fig. S2, C and E) were used to calculate the bell morphologies for Eq. 6. In addition to validating the model with experimental data, parameter sweeps were conducted according to the values in table S2. Additional information and results from parameter sweeps are included in Supplementary Text and figs. S2 to S4.

Mechanistic model for COT
The mechanistic model COT was calculated using the resulting thrust per mass with the following geometric inputs for a fineness ratio of 0.3 to match experimental data: $d_r = 20$ cm, $\Delta d = 10$ cm, $h_r = 6$ cm, $\Delta h = 2$ cm, $h_j = 3$ cm, $t_c = 0.4$ s, $t_r = 1.4$ s, and $s = 1$. No experimental data were used to calculate mechanistic model COTs.

SUPPLEMENTARY MATERIALS
Supplementary material for this article is available at http://advances.sciencemag.org/cgi/content/full/6/5/eaaz3194/DC1
Supplementary Text
Fig. S1. Muscle orientation along the subumbrellar surface.
Fig. S2. Details of the adapted hydrodynamic model.
Fig. S3. Parametric dependencies of enhanced propulsion.
Fig. S4. Additional parametric dependencies of enhanced propulsion model parameter sweeps.
Fig. S5. Power requirements of the microelectronic system versus animal.
Table S1. Experimental parameters (columns) for each electrical signal characteristic test (rows).
Table S2. Model parameters, including the resting body diameter (d_r), range of diameters between relaxation and contraction geometries (Δd), resting body height (h_r), range of height between contraction and relaxation geometries (Δd), tissue height or depth (h_j), contraction

time (t_c), relaxation time (t_r), and a geometric scale factor (s) that factors into each geometric parameter proportionally.

Table S3. External power per mass calculations of various robotic constructs.

Movie S1. A comparison of bell geometries for unstimulated swimming with an inactive swim controller embedded (left) and externally controlled swimming at 0.50 Hz (middle) and 0.88 Hz (right).

References (43)

REFERENCES AND NOTES

1. B. J. Gemmell, J. H. Costello, S. P. Colin, C. J. Stewart, J. O. Dabiri, D. Tafti, S. Priya, Passive energy recapture in jellyfish contributes to propulsive advantage over other metazoans. *Proc. Natl. Acad. Sci. U.S.A.* **110**, 17904–17909 (2013).

2. Y. Tadesse, A. Villanueva, C. Haines, D. Novitski, R. Baughman, S. Priya, Hydrogen-fuel-powered bell segments of biomimetic jellyfish. *Smart Mater. Struct.* **21**, 045013 (2012).

3. A. Villanueva, C. Smith, S. Priya, A biomimetic robotic jellyfish (Robojelly) actuated by shape memory allow composite actuators. *Bioinspir. Biomim.* **6**, 036004 (2011).

4. A. Villanueva, P. Vlachos, S. Priya, Flexible margin kinematics and vortex formation of *Aurelia aurita* and Robojelly. *PLOS ONE* **9**, e98310 (2014).

5. S.-W. Yeom, I.-K. Oh, A biomimetic jellyfish robot based on ionic polymer metal composite actuators. *Smart Mater. Struct.* **18**, 085002 (2009).

6. K. Marut, C. Stewart, T. Michael, A. Villanueva, S. Priya, A jellyfish-inspired jet propulsion robot actuated by an iris mechanism. *Smart Mater. Struct.* **22**, 094021 (2013).

7. T. Li, G. Li, Y. Liang, T. Cheng, J. Dai, X. Yang, B. Liu, Z. Zeng, Z. Huang, Y. Luo, T. Xie, W. Yang, Fast-moving soft electronic fish. *Sci. Adv.* **3**, e1602045 (2017).

8. G.-Z. Yang, J. Bellingham, P. E. Dupont, P. Fischer, L. Floridi, R. Full, N. Jacobstein, V. Kumar, M. McNutt, R. Merrifield, B. J. Nelson, B. Scassellati, M. Taddeo, R. Taylor, M. Veloso, Z. L. Wang, R. Wood, The grand challenges of *Science Robotics*. *Sci. Robot.* **3**, eaar7650 (2018).

9. J. C. Nawroth, H. Lee, A. W. Feinberg, C. M. Ripplinger, M. L. McCain, A. Grosberg, J. O. Dabiri, K. K. Parker, A tissue-engineered jellyfish with biomimetic propulsion. *Nat. Biotechnol.* **30**, 792–797 (2012).

10. S.-J. Park, M. Gazzola, K. S. Park, S. Park, V. Di Santo, E. L. Blevins, J. U. Lind, P. J. Campbell, S. Dauth, A. K. Capulli, F. S. Pasqualini, S. Ahn, A. Cho, H. Yuan, B. M. Maoz, R. Vijaykumar, J.-W. Choi, K. Deisseroth, G. V. Lauder, L. Mahadevan, K. K. Parker, Phototactic guidance of a tissue-engineered soft-robotic ray. *Science* **353**, 158–162 (2016).

11. Y. Morimoto, H. Onoe, S. Takeuchi, Biohybrid robot powered by an antagonistic pair of skeletal muscle tissues. *Sci. Robot.* **3**, eaat4440 (2018).

12. V. A. Webster, E. L. Hawley, O. Akkus, H. J. Chiel, R. D. Quinn, Effect of actuating cell source on locomotion of organic living machines with electrocompacted collagen skeleton. *Bioinspir. Biomim.* **11**, 036012 (2016).

13. V. A. Webster, K. J. Chapin, E. L. Hawley, J. M. Patel, O. Akkus, H. J. Chiel, R. D. Quinn, *Aplysia californica* as a novel source of material for biohybrid robots and organic machines, in *Biomimetic and Biohybrid Systems. Living Machines 2016. Lecture Notes in Computer Science*, N. Lepora, A. Mura, M. Mangan, P. Verschure, M. Desmulliez, T. Prescott, Eds. (Springer, 2016), vol. 9793.

14. C.-H. Lucas, Reproduction and life history strategies of the common jellyfish, *Aurelia aurita*, in relation to its ambient environment. *Hydrobiologia* **451**, 229–246 (2001).

15. NOAA Ship Okeanos Explorer, 2016 Expeditions Overview; https://oceanexplorer.noaa.gov/okeanos/explorations/2016-overview/welcome.html [accessed June 2019].

16. F. Roquet, L. Boehme, B. Block, J. B. Charrasin, D. Costa, C. Guinet, R. G. Harcourt, M. A. Hindell, L. A. Hückstädt, C. R. McMahon, B. Woodward, M. A. Fedak, Ocean observations using tagged animals. *Oceanography* **30**, 139 (2017).

17. J. B. J. Harvey, J. P. Ryan, R. Marin, C. M. Preston, N. Alvarado, C. A. Scholin, R. C. Vrijenhoek, Robotic sampling, in situ monitoring and molecular detection of marine zooplankton. *J. Exp. Mar. Biol. Ecol.* **413**, 60–70 (2012).

18. J. P. Egerton, A. F. Johnson, J. Turner, L. LeVay, I. Mascarenas-Osorio, O. Aburto-Oropeza, Hydroacoustics as a tool to examine the effects of Marine Protected Areas and habitat type on marine fish communities. *Sci. Rep.* **8**, 47 (2018).

19. G. Herschlag, L. Miller, Reynolds number limits for jet propulsion: A numerical study of simplified jellyfish. *J. Theor. Biol.* **285**, 84–95 (2011).

20. M. J. McHenry, J. Jed, The ontogenetic scaling of hydrodynamics and swimming performance in jellyfish (*Aurelia aurita*). *J. Exp. Biol.* **206**, 4125–4137 (2003).

21. M. N. Arai, *A Functional Biology of Scyphozoa* (Chapman & Hall, 1997).

22. W. G. Gladfelter, A comparative analysis of the locomotory systems of medusoid *Cnidaria*. *Helgolander Wiss. Meersunters.* **25**, 228–272 (1973).

23. S. Fossette, A. C. Gleiss, J. Chalumeau, T. Bastian, C. D. Armstrong, S. Vandenabeele, M. Karpytchev, G. C. Hays, Current-oriented swimming by jellyfish and its role in bloom maintenance. *Curr. Biol.* **25**, 342–347 (2015).

24. G. A. Horridge, The nerves and muscles of medusae. I. Conduction in the nervous system of *Aurelia aurita* Lamarck. *J. Exp. Biol.* **31**, 594 (1954).

25. G. J. Romanes, The Croonian Lecture: Preliminary observations on the locomotor system of medusae. *Philos. Trans. R. Soc. Lond.* **166**, 269–313 (1876).

26. B. J. Gemmell, S. P. Colin, J. H. Costello, J. O. Dabiri, Suction-based propulsion as a basis for efficient animal swimming. *Nat. Commun.* **6**, 8790 (2015).

27. G. O. Mackie, R. W. Meech, Central circuitry in the jellyfish *Aglantha digitale* II. The ring giant and carrier systems. *J. Exp. Biol.* **198**, 2271–2278 (1995).

28. D. M. Chapman, Microanatomy of the bell rim of *Aurelia aurita* (Cnidaria: Scyphozoa). *Can. J. Zool.* **77**, 34–46 (1999).

29. L. M. Passano, Pacemakers and activity patterns in medusae: Homage to Romanes. *Am. Zool.* **5**, 465–481 (1965).

30. R. A. Satterlie, Neuronal control of swimming in jellyfish: A comparative story. *Can. J. Zool.* **80**, 1654–1669 (2002).

31. G. L. Romanes, Concluding observations on the locomotor system of medusae. *Philos. Trans. R. Soc. Lond.* **Part I**, 352 (1879).

32. T. H. Bullock, Facilitation in Medusae. *J. Cell. Comp. Physiol.* **22**, 251–272 (1943).

33. J. Frame, N. Lopez, O. Curet, E. D. Engeberg, Thrust force characterization of free-swimming soft robotic jellyfish. *Bioinspir. Biomim.* **13**, 064001 (2018).

34. R. K. Katzschmann, J. DelPreto, R. MacCurdy, D. Rus, Exploration of underwater life with an acoustically controlled soft robotic fish. *Sci. Robot.* **3**, eaar3449 (2018).

35. Hydroid Inc., Hydroid introduces the new generation REMUS 100 AUV; https://www.hydroid.com/news/hydroid-introduces-new-generation-remus-100-auv [accessed June 2019].

36. J. O. Dabiri, S. P. Colin, J. H. Costello, M. Gharib, Flow patterns generated by oblate medusan jellyfish: Field measurements and laboratory analyses. *J. Exp. Biol.* **208**, 1257–1265 (2005).

37. J. O. Dabiri, Optimal vortex formation as a unifying principle in biological propulsion vortex formation time: The dimensionless timescale during which vortex formation occurs. *Annu. Rev. Fluid Mech.* **41**, 17–33 (2009).

38. J. O. Dabiri, S. P. Colin, K. Katija, J. H. Costello, A wake-based correlate of swimming performance and foraging behavior in seven co-occurring jellyfish species. *J. Exp. Biol.* **213**, 1217–1225 (2010).

39. M. J. Abrams, T. Basinger, W. Yuan, C.-L. Guo, L. Goentoro, Self-repairing symmetry in jellyfish through mechanically driven reorganization. *Proc. Natl. Acad. Sci. U.S.A.* **112**, E3365–E3373 (2015).

40. D. Yuan, N. Nakanishi, D. K. Jacobs, V. Hartenstein, Embryonic development and metamorphosis of the scyphozoan *Aurelia*. *Dev. Genes Evol.* **218**, 525–539 (2008).

41. R. J. Larson, Trophic ecology of planktonic gelatinous predators in Saanich Inlet, British Columbia: Diets and prey selection. *J. Plankton Res.* **9**, 811–820 (1987).

42. T. L. Daniel, Mechanics and energetics of medusan jet propulsion. *Can. J. Zool.* **61**, 1406–1420 (1983).

43. B. Lee, P. Messersmith, J. Israelachvili, J. Waite, Mussel-inspired adhesives and coatings. *Ann. Rev. Matl. Res.* **41**, 99–132 (2011).

Citation: N. W. Xu, J. O. Dabiri, Low-power microelectronics embedded in live jellyfish enhance propulsion. *Sci. Adv.* **6**, eaaz3194 (2020).

Science Advances

Low-power microelectronics embedded in live jellyfish enhance propulsion

Nicole W. Xu and John O. Dabiri

ARTICLE TOOLS	http://advances.sciencemag.org/content/6/5/eaaz3194
SUPPLEMENTARY MATERIALS	http://advances.sciencemag.org/content/suppl/2020/01/27/6.5.eaaz3194.DC1
REFERENCES	This article cites 39 articles, 9 of which you can access for free http://advances.sciencemag.org/content/6/5/eaaz3194#BIBL
PERMISSIONS	http://www.sciencemag.org/help/reprints-and-permissions

Use of this article is subject to the Terms of Service